Cite as:
A Camara, LE Fernandez-Elvira, C Stroumpouli, C Jagadeesh (2023).
Skew wind actions on vehicles crossing bridges with solid parapets.
Journal of Wind Engineering and Industrial Aerodynamics 240, 105485

Skew wind actions on vehicles crossing bridges with solid parapets

Alfredo Camara[a], Luis Fernandez Elvira[b], Chrysanthi Stroumpouli[b], Chetan Jagadeesh[b]

[a]*Department of Continuum Mechanics and Theory of Structures, Universidad Politécnica de Madrid, Calle Profesor Aranguren s/n, 28040 Madrid, Spain.*
[b]*Department of Civil Engineering. City, University of London. Northampton Square, London, EC1V 0HB, United Kingdom*

Abstract

This work focuses on the effect that the angle of incidence of the wind has on the flow around bridge decks with low-rise edge parapets, and how it affects the aerodynamic actions on vehicles. First, a generic deck model with different barrier configurations is studied using computational fluid dynamic (CFD) analysis, and it is observed that for very skew winds even relatively low barriers can deviate the flow to make it aligned with the direction of the deck, which is referred to as channelling effect in this study. The work continues with an extensive wind tunnel (WT) testing programme on a deck model that represents a realistic bridge with a conventional configuration of short side barriers. The flow visualisation and the aerodynamic forces measured on a high-sided vehicle show the existence of three different zones in terms of the skew angle of the wind, which are in agreement with the CFD results. It is concluded that skew winds can significantly increase the aerodynamic actions on the vehicles due to the reduction of the shielding area across the width of the deck, and also because of the along-deck wind channelling.

Keywords:
Skew winds; wind tunnel testing; high-sided vehicles; bridge aerodynamics; CFD; aerodynamic coefficients

Email address: alfredo.camara@upm.es (Alfredo Camara)

Nomenclature

α^*	Apparent wind incidence angle in the test with x_v northbound.
α	Angle between the horizontal mean wind speed and the deck.
$\bar{P}_i$	Time-averaged pressure at the i-th pressure tap on the vehicle.
$\bar{U}$	Time-averaged wind speed.
β	Relative incidence angle between the wind and a moving vehicle.
γ	Inclination of the horizontal wind vector along the deck.
ν_a	Kinematic viscosity of air.
ψ	Angle between the mean wind speed at the inlet and the horizontal wind force resultant on the vehicle.
ρ	Density of air.
σ_u	Standard deviation of the stream-wise turbulence.
Re	Reynolds number.
A_f	Area of the rear face of the vehicle.
A_i	Tributary area corresponding to the i-th pressure tap on the vehicle.
C_j	Aerodynamic coefficient of the vehicle, with $j = S, D, R, P, Y$ referring to the side, drag, rolling, pitching and yawing, respectively.
d	Depth of the deck (without considering the barriers).
f	Frequency.
F_j	Drag ($j = D$) and side ($j = S$) force on the vehicle.
h	Vertical distance between the bottom of the vehicle and its centroid.
h_f	Height of the side barriers of the deck.
H_v	Total height of the vehicle.
H_{obs}	Depth of the deck including the side barriers.

H_{vo} Height of the vortex generators in the wind tunnel.

L_u Length scale of the stream-wise turbulence.

L_v Total length of the vehicle.

M_j Rolling, pitching and yawing moments on the vehicle, with $j = R, P, Y$, respectively.

$n_i^{x_v}, n_i^{y_v}, n_i^{z_v}$ Components of the vector normal to the surface of the vehicle in the i-th pressure tap.

N_t Number of pressure taps in the vehicle.

P_i Pressure at the i-th pressure tap on the vehicle.

S_u Auto-spectral density of the stream-wise turbulence.

t Time.

U_h Magnitude of the horizontal component of the wind velocity vector.

U_x Mean wind speed in the x direction (along-flow).

U_z Mean wind speed in the z direction (across-flow horizontal).

U_W Free-stream wind velocity in the wind tunnel.

$U_{x,\infty}$ Horizontal mean wind speed in the inlet.

V Vehicle speed.

W_v Total width of the vehicle.

x_G, y_G, z_G Coordinates of the centroid of the vehicle in its local axes.

x_i, y_i, z_i Coordinates of the i-th pressure tap in the local vehicle axes.

x_v, y_v, z_v Local axes of the vehicle.

z Height from the floor of the wind tunnel.

1. Introduction

Wind causes a large number of accidents and interruptions on road and railway networks, particularly on bridges because of their exposure [1, 2, 3]. Understanding the aerodynamic actions on vehicles crossing bridges is essential to assess the risk of accidents and discomfort.

Many researchers have studied the on-bridge vehicle wind actions in bridges under purely crosswinds. Wind tunnel (WT) testing programmes have demonstrated the importance that the flow interference created by the shape of the deck and its furniture (parapets, wind barriers, etc.) have on trains [4, 5, 6] and road vehicles [3, 7, 8, 9, 10, 11]. Although these works consider the mean wind speed perpendicular to the deck, skew winds that form an angle $\alpha \neq 90^\circ$ with respect to the deck are more likely to occur, and they are usually more dangerous from the point of view of the vehicle stability [12, 13, 14, 15]. In addition, the combination of the vehicle speed (V) and the mean wind speed ($U_{x,\infty}$) results in a relative yaw incidence angle β as shown in Fig. 1(a), even for purely orthogonal winds. Indeed, Baker [16] demonstrated with a dynamic model of a 4-wheeled vehicle that yaw angles between $\beta = 30^\circ$ and 60° (headwinds) are more dangerous for the driving stability of high-sided vehicles situated in homogeneous wind fields free from obstacles (i.e. in off-bridge conditions). The same conclusion was reached in the static analysis of different types of vehicles on a long-span bridge conducted by Kim *et al.* [17]. Recently, Camara [18] proposed a dynamic wind-vehicle-bridge interaction model that incorporated skew wind velocity histories and concluded that headwinds in the range between $\beta = 40^\circ$ and 70° maximise the risk of driving accidents. The previous studies are based on off-bridge aerodynamic vehicle coefficients, which are also used in many other works focusing on the driving safety and comfort in bridges under wind actions (e.g. [19, 20, 21, 22]). However, Han *et. al.* [23] demonstrated the existence of significant flow interferences of the deck on the vehicle, and the importance of obtaining the on-bridge vehicle aerodynamic coefficients for a wide range of skew angles. Such disturbances may also deviate the projection of the wind direction in the horizontal plane along the deck, as well as the resultant horizontal aerodynamic force on the vehicles, described by the angles γ and ψ in Figs. 1(b) and (c), respectively.

Cheli *et al.* [24] compared the off-bridge and on-bridge wind actions in WT experiments of a relatively shallow railway bridge without furniture, and they did not report significant variations of the results for different yaw

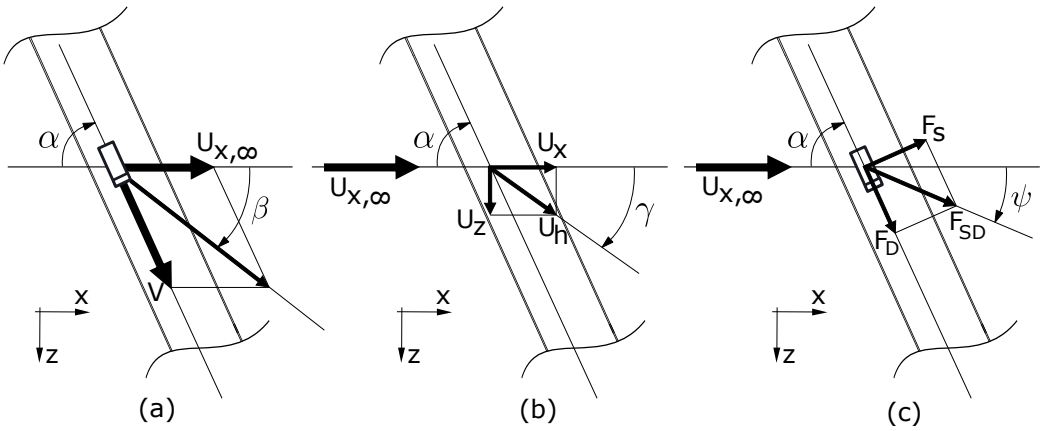

Figure 1: Definition and positive convention of representative angles in bridges under skew wind actions: (a) relative incidence angle β of wind on a moving vehicle, (b) inclination γ of the horizontal wind vector along the deck, (c) angle ψ between the mean wind speed and the horizontal wind force resultant.

angles. This is in agreement with the work of Dorigatti *et al.* [25], who tested a typical long-span road bridge deck subject to a limited range of wind skew angles from $\alpha = 60°$ to $120°$. They considered a bridge deck with relatively small parapets, in which the ratio of their height (h_f) and the depth of the deck (d) is less than 0.25. However, in a different work Cheli *et al.* [26] studied experimentally single- and double-deck road bridges with larger railed parapets ($h_f/d \approx 0.5$), and it was observed that the bridge interference modifies the lateral force and rolling moment coefficients of the vehicles, particularly when the skew angle is significant ($\alpha = 45°$) and the width of the deck is narrow. Although it was not specifically explored by these authors, their measurements could have been affected by the along-deck wind flow deviated by deck and its furniture for skew angles, referred to as 'channelling effect' in the present work. Relatively narrow bridges with large solid windward barriers ($h_f/d \approx 1.2$ and 2) were tested by Kozmar *et al.* [27], and they argued that the skew angle of wind does not seem to affect the flow field characteristics significantly. This could be attributed to the lack of leeward barriers, which can redirect the wind flow along the deck as it is demonstrated in the present work.

More recently, WT testing with scaled moving vehicles conducted at Southwest Jiaotong University confirmed the strong influence of the skew wind angle on the flow structures along different types of decks, including

a through-truss deck with significant wind shielding [28, 29], and a shallow box girder with or without windward barriers ($h_f/d = 0.7$) [30, 31]. Despite the different levels of shielding considered in these studies it was concluded that the aerodynamic coefficients of the vehicles on the deck were not only affected by the relative incidence angle of the wind (or yaw angle β), as it is the case in off-bridge conditions, but also by the skew wind angle (α) given its influence on the flow interferences introduced by the deck. The effect of the shape of the super-structure on the skew wind actions on the vehicles was also observed by other researchers experimentally [32, 33, 34] and numerically with computational fluid dynamic (CFD) analysis [35, 36], but it has not been clearly connected with the parapets of the deck and their potential channelling effect.

Solid parapets are widely used for safety, construction and maintenance of bridges. The aim of this paper is to explore their effect on skew wind flows around the deck, and also on the resulting vehicle aerodynamic actions. To this end, the study combines CFD and WT testing on typical prestressed concrete bridge decks. First, an extensive three-dimensional CFD analysis is conducted on a highly idealised deck model to assess the influence that the skew angle α has on the along-deck wind flow of the deck, considering different configurations of the edge barriers. The results indicate the existence of three distinct zones of influence of α on the wind velocity vector along the deck, which is almost aligned with the deck within the height of the barriers when $\alpha < 60°$ or $\alpha > 120°$. This is due to the windward barrier and the results are in agreement with the WT testing conducted in a detailed scaled model of a real bridge. In these experiments, the flow visualisation and the study of the pressure maps and the resultant forces on the vehicles clearly indicate the importance of the wind skew angle on the driving safety due to the along-deck flow channelling effects.

2. Bridge cross-sections

Two different road bridge box girders are examined in this work: (1) a 'generic' idealised deck cross-section that is studied numerically using CFD, and (2) a 'typical' deck shape corresponding to a real bridge that is studied experimentally in a WT. Both cases are illustrated in Fig. 2, in which the dimensions have been normalised with respect to the depth of the deck (d). In order to minimise local flow perturbations, and to focus on the effect of the bridge furniture on the wind field above the deck in the generic bridge model

of Fig. 2(a), it has been simplified to a single box girder, a top slab with uniform thickness ($0.09d$) and two edge parapets. The deck cross-section in Fig. 2(b) represents a typical prestressed concrete bridge with double box girder. Its detailed dimensions are taken from the midspan cross-section of the Orwell Bridge (UK, 190-m main span) and it has 4 lanes (L1 - L4), two of them in the upwind girder (UG) and the other two in the downwind girder (DG). The solid parapets in both cross-sections have a height of $h_f = d/3$, which is representative of many long-span bridges with concrete barriers, or with edge parapets formed by a concrete plinth and metal railing on top [37].

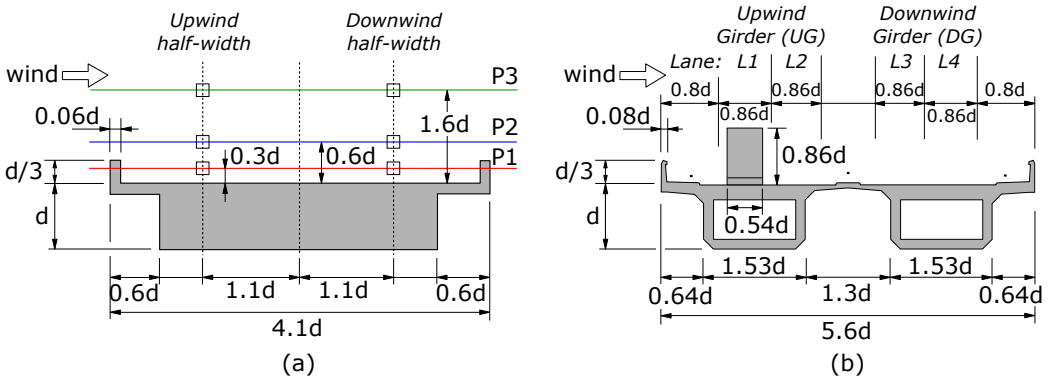

Figure 2: Dimensions of the bridge cross-sections in terms of their depth d: (a) idealised generic bridge, (b) typical bridge with a high-sided vehicle.

3. Numerical study of deck channeling effects

The aim of this section is to characterise the diverting effect of the deck and its parapets on the mean wind field across its width. To this end, series of three-dimensional (3D) CFD finite volume analyses were conducted in OpenFOAM [38] considering the idealised deck model presented in Fig. 2(a). In this model we chose $d = 154$ mm to assimilate it to the WT experiments presented later. Vehicles are not included in the numerical model to focus on the flow around the deck.

In the CFD analysis the Reynolds-averaged Navier–Stokes (RANS) equations and the standard $k-\epsilon$ turbulence model [39] are solved in steady state. This is deemed appropriate considering that the goal of the CFD analysis in this research is to visualise the global wind flow around the deck for different skew angles, and not to calculate the transient aerodynamic actions. For this

reason, wall functions that incorporate the linear (laminar) and logarithmic (turbulent) law-of-the-wall are implemented close to the deck surface with $y^+ \approx 50$ in the first grid cell, spanning the inner region between the wall and the fully developed turbulence region. The pressure-velocity coupling of the fluid motion equations is solved with the semi-implicit algorithm SIMPLE [40].

The 3D fluid domain around the deck model is described in Fig. 3(a) in terms of the depth of the deck plus the side barriers ($H_{obs} = d + h_f = 4d/3$). Sensitivity analysis were performed to validate the width of the fluid domain and its near-wall refinement. The shape of the fluid cells is hexaedral (structured) in the whole domain, establishing 7 inflation layers around the perimeter of the deck that have a thickness of 1 mm in the first layer and grow with an expansion rate of 1.2. A detail of the mesh close to the perimeter of the deck cross-section is included in Fig. 3(b). The values of the skew wind angle considered range from $\alpha = 20°$ to 90°, typically with increments of 10°. As a reference, the model with purely orthogonal wind ($\alpha = 90°$) and both edge barriers has approximately 4 million cells in the fluid domain. The different wind incidence angles are achieved by rotating the deck with respect to the y axis and maintaining the orientation of the boundary conditions of the flow. This implies that the mesh varies from case to case, but its resolution is maintained and it has been verified that re-meshing for different wind skew angles does not affect significantly the results.

Fig. 3(a) also includes the reference axes of coordinates and the boundary conditions applied to all the faces, with a uniform wind flow of $U_{x,\infty} = 10$ m/s in the x direction imposed at the inlet ($\mathrm{Re} = U_{x,\infty} d/\nu_a \approx 1.5 \times 10^5$, with $\nu_a = 1.48 \times 10^{-5}$ m^2/s being the kinematic viscosity of air). Several variations of the barrier configuration presented in Fig. 2(a) are introduced to study their effect on the flow, resulting in the following cases: (1) original model with the two edge parapets, (2) model with only the windward parapet, and (3) model with no parapets. The three deck cross-sections are shown in Fig. 4.

3.1. Across-flow horizontal wind field

Fig. 4 presents the across-flow horizontal wind field (U_z) in the vertical $x-y$ midplane of the model illustrated in Fig. 3(a). The results are normalised with respect to the inlet wind speed $U_{x,\infty} = 10$ m/s to show the important influence of the angle between the deck and the mean wind speed on the deviation of the flow. When the wind direction is purely orthogonal to the

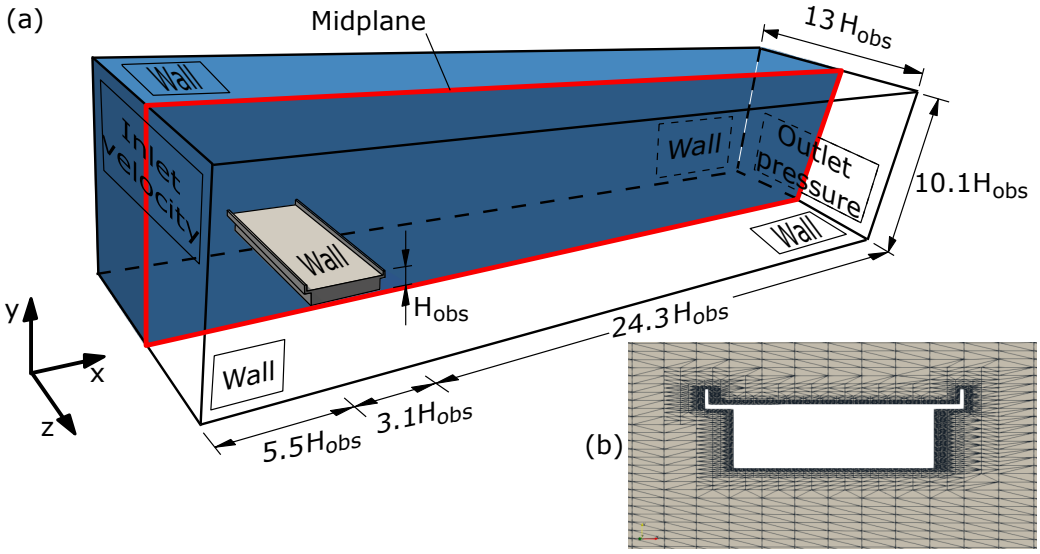

Figure 3: (a) Geometry and boundary conditions of the CFD study in the generic bridge section. $H_{obs} = 4d/3$ is the total depth of the deck, including the edge barriers. The blue shaded region represents half of the wind domain, the other half is removed for visualisation purposes. (b) Detail of the mesh around the cross-section of the deck. The two views correspond to the case with $\alpha = 90°$ and both barriers.

deck the across-flow component of the wind field (U_z) is negligible, regardless of the barrier arrangement above the deck slab, as it is observed in Figs. 4(a) - (c). However, skew winds forming an angle of $\alpha = 45°$ with the deck are partly diverted when they reach the vertical faces of the girder, which creates a U_z component of the wind velocity vector that is up to 70% of the inlet speed. This effect is observed along the depth of the deck (d) regardless of its barriers, but the presence of a windward edge parapet extends it above the pavement and reach the region used by the vehicles. This is shown in Figs. 4(d) and (e), which also indicate that the leeward parapet does not contribute to the diversion of the wind flow in the carriageways.

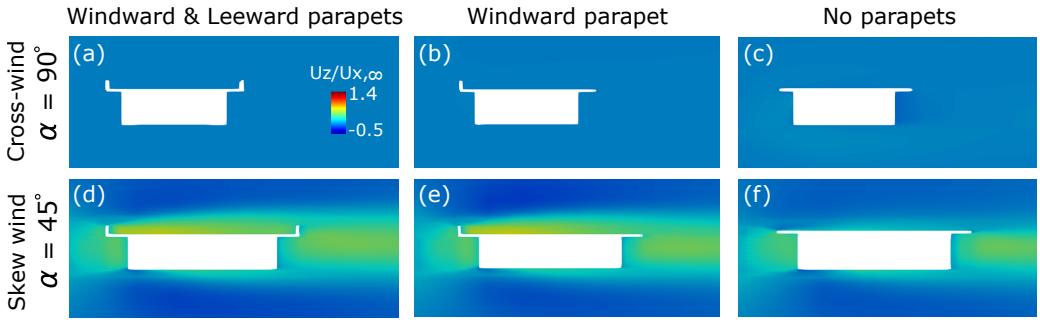

Figure 4: Normalised across-wind velocity fields ($U_z/U_{x,\infty}$) for different wind incidence angles and geometries of the generic bridge cross-section.

3.2. Deck channelling effects

The across-wind velocity field U_z included in Fig. 4 is strongly influenced by the distance above the deck in which it is measured. In order to explore this effect and the orientation of the wind flow along the deck, the wind speed is obtained in the horizontal $x-z$ planes P1, P2 and P3 described in Fig. 2(a). Each of these planes contain the interpolated CFD results corresponding to the fluid cells that they intersect. Ignoring the y-component of the wind velocity gives a grid of points in each horizontal plane with velocities in the x and z directions (U_x and U_z, respectively). We define the along-deck horizontal inclination of the wind field shown in Fig. 1(b) as:

$$\gamma = \arctan\left(\frac{U_z}{U_x}\right). \tag{1}$$

The angle of wind above the deck γ is calculated along two lines parallel to the bridge that are located at the centres of the upwind and the downwind halves of its width, as shown in Fig. 2(a). This is done for each of the planes P1-P3, and the arithmetic average of γ along these lines is calculated discarding the points close to the $x-y$ boundary faces. Fig. 5(a) shows the averaged γ in the plane P1 of the model with two edge barriers. The results indicate that purely cross-winds with $\alpha = 90°$ lead to $\gamma = 0°$. This means that the streamlines are contained in vertical $x-y$ planes, and it is visualised in the quiver plot presented in Fig. 5(b) when $\alpha = 90°$, in which the size of the vectors represents the magnitude of the horizontal wind component (i.e. $U_h = \sqrt{U_x^2 + U_z^2}$ in Fig. 1(b)), and their inclination is given by γ. Fig. 5(b) also shows the small magnitude of the horizontal wind velocity within the edge parapets due to their shielding effect for purely cross-winds. However, for non-orthogonal winds the horizontal inclination of flow along the deck within the height of the parapets is significant, and its relationship with the incidence angle α can be divided in three zones represented in Fig. 5(a):

- Zone I - Initiation of channelling. This region corresponds to nearly-orthogonal winds with $75° < \alpha < 90°$, for which the angle of wind along the deck (γ) is very sensitive to α. As the wind incidence angle is more skewed with respect to the deck the wind field across its width rapidly becomes more aligned with the direction of its edge barriers, particularly in the upwind half of the deck. Fig. 5(c) shows the horizontal wind field for a representative incidence angle in this region.

- Zone II - Transition. When $60° < \alpha < 75°$ the inclination of wind along the deck is almost insensitive to variations of the skew wind angle. In this region, as the incident wind becomes more parallel to the deck (i.e. α is reduced) the flow within the height of the edge barriers is almost aligned with them, as shown in Fig. 5(d) .

- Zone III - Full channelling. If the wind is significantly skewed, with $\alpha < 60°$, the windward barrier diverts the streamlines and creates a strong wind flow parallel to the girder in the first half of the deck, introducing a full channelling effect for which $\gamma \approx \alpha$. This effect is less pronounced in the downwind half of the deck after the streamlines reattach, as it is illustrated in Fig. 5(e). The quiver plot also shows that the magnitude of the horizontal wind field along the deck for very skew winds is larger than for orthogonal flows, suggesting the loss of

the shielding effect of the edge barriers in Zone III. The limit case in which $\alpha = 0°$ has not been analysed due to modelling difficulties, but in this case the deck is parallel to the wind flow and therefore it would lead to $\gamma = 0°$ across its width.

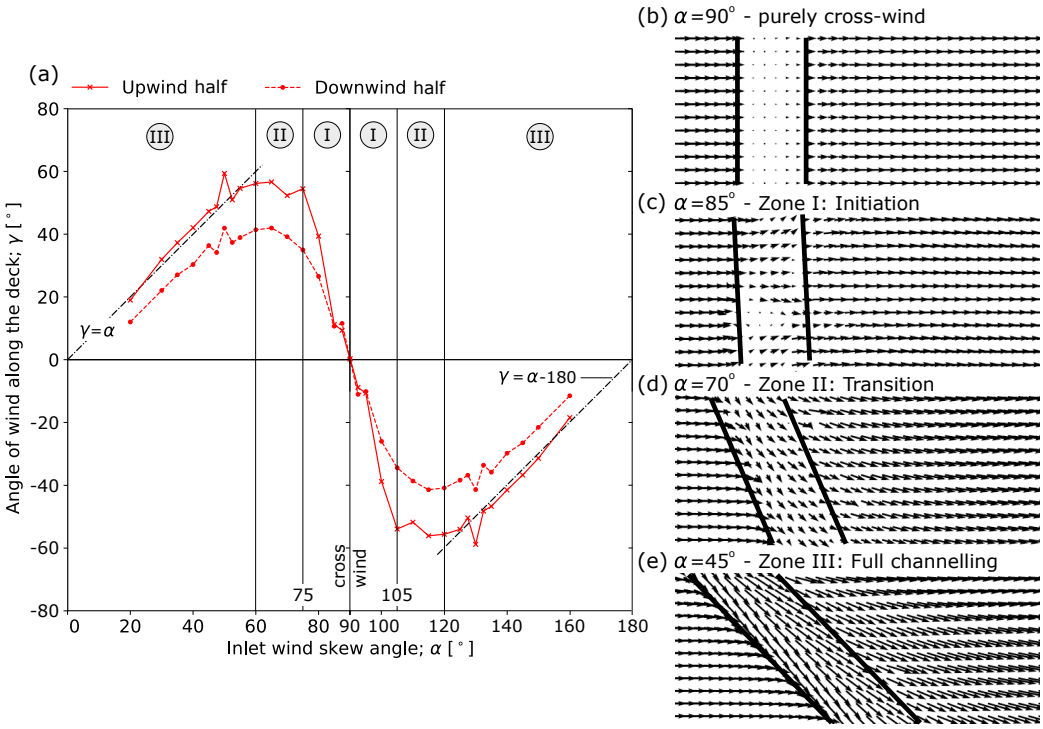

Figure 5: (a) Horizontal inclination of the wind velocity vector along the deck (γ) for different wind incidence angles α in the plane P1, within the height of the barriers. Figures (b)-(e) include quiver plots with the horizontal wind vector orientation around the deck, with the thick black lines indicating its edge barriers (plan view of the deck). CFD results in the generic bridge with both edge barriers.

If the wind skew angle is $\alpha > 90°$ the values of the angle γ are anti-symmetric with respect to the axis $\alpha = 90°$, and the full channelling region is described by $\gamma \approx \alpha - 180°$, as it is indicated in Fig. 5(a).

The above zonification refers to the plane P1 in the bridge with both edge barriers. Fig. 6 compares the averaged wind inclination γ in different planes and deck cross-sections. The angle γ in the plane closer to the upper slab of the bridge (P1) obtained for the case with the two edge barriers is almost

identical to the case with only the windward parapet, distinguishing the three regions of channelling previously discussed (Figs. 6(a) and Fig. 6(b)). However, the deviation of the wind field above the deck is small when there are no barriers on the deck ($\gamma \approx 0$ for any value of the skew wind angle α), even in the plane P1 as shown in Fig. 6(c). On the other hand, the influence of the furniture of the bridge above the deck is less significant as the distance from the pavement level increases. Certain flow channelling is observed in the downwind half of the bridge with barriers in the intermediate plane P2, but this effect disappears in plane P3, which corresponds to height of the top of typical high-sided vehicles, regardless of the presence of parapets.

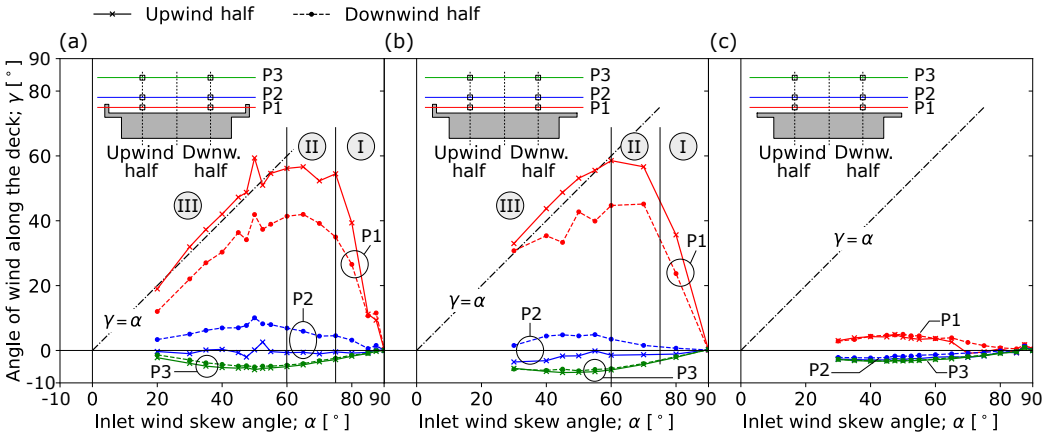

Figure 6: Horizontal inclination of the wind velocity vector along the deck (γ) for different wind incidence angles α in the bridge section with (a) both edge parapets, (b) windward parapet, and (c) no parapets. CFD results in different horizontal planes (P1-P3) of the generic bridge.

The magnitude of the horizontal wind field is also affected by the flow channelling in the models with windward barriers, as it is shown in the along-deck average of U_h presented in Figs. 7(a) and (b). This is appreciable in the plane P1, where the velocity magnitude is reduced due to the protection of the barriers if the wind is nearly orthogonal to the deck (Zone I), and it gets closer to the inlet wind speed as the wind incidence angle is more skewed (Zones II and III). The channelling effect in terms of U_h is smaller in plane 2 (but higher than in terms of γ at this position), and it vanishes in plane P3. The influence of α in the velocity magnitude is also weak in the bridge without parapets described in Fig. 7(c), regardless of the position above the deck where it is measured.

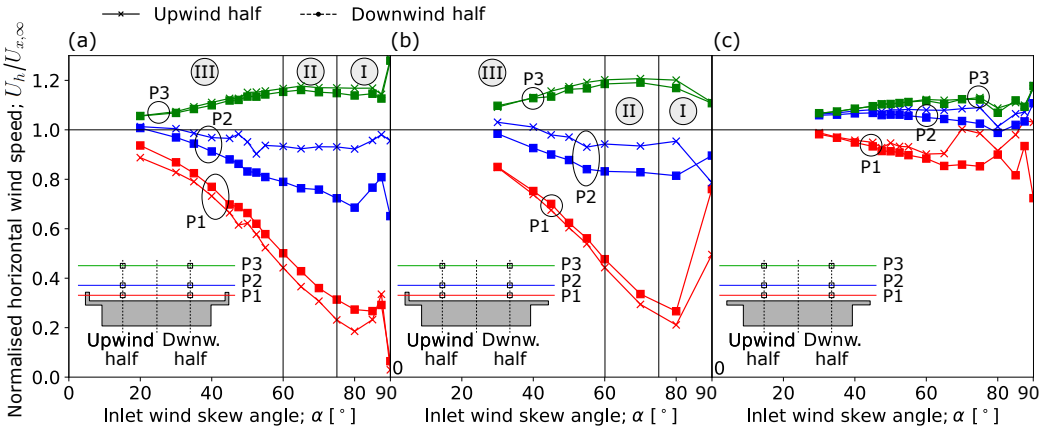

Figure 7: Horizontal wind speed magnitude along the deck (U_h) normalised with respect to the inlet wind speed ($U_{x,\infty}$) for different wind incidence angles α in the bridge section with (a) both edge parapets, (b) windward parapet, and (c) no parapets. CFD results in different horizontal planes (P1-P3) of the generic bridge.

4. Experimental testing of a typical deck with a high-sided vehicle

The purpose of the WT testing is to study the wind flow around the deck of a typical bridge and the aerodynamic forces on high-sided vehicles for different wind incidence angles. To this end, a 1/50 scale model of the midspan segment of the bridge deck included in Fig. 2(b) was built and tested in the closed-return environmental WT at City, University of London.

4.1. Preliminary considerations

The working zone of the WT is 3-m wide x 1.5-m high x 8.1-m long. A castellated barrier and four elliptical vortex generators with a height of $H_{vo} = 1.2$ m were fitted at the upstream end of the working zone to generate simulated atmospheric shear flows. These were described in detail by Sykes [41]. In addition, the floor between the vortex generators and the 2.8-m diameter turning table was covered by near-cylindrical roughness elements, with height of 70 mm ($0.058H_{vo}$) and mean diameter of 55 mm.

First, the wind field at the centre of the rotary table was measured without the deck model, with a free-stream wind speed of $U_W = 9$ m/s. The measurements were obtained in 248 points equally-spaced in the vertical direction (z) using a pressure scanner mounted on an adjustable rake. The sampling time and frequency was 600 s and 100 Hz, respectively. Fig. 8(a) shows the profiles of the time-averaged horizontal (stream-wise) velocity and

turbulence intensity, normalised with respect to the height of the vortex generators (H_{vo}) and the free-stream wind speed (U_W). The measured boundary layer can be described by the power law

$$\frac{\bar{U}}{U_W} = \left(\frac{z}{H_{vo}}\right)^{0.25}, \tag{2}$$

with $\bar{U}$ representing the time-average of the wind speed and z the distance from the tunnel floor. This work is mostly interested in the wind flow around the deck of the bridge, where the boundary layer also matches the profile given by EN1991-1-4 [42] for a terrain of type II.

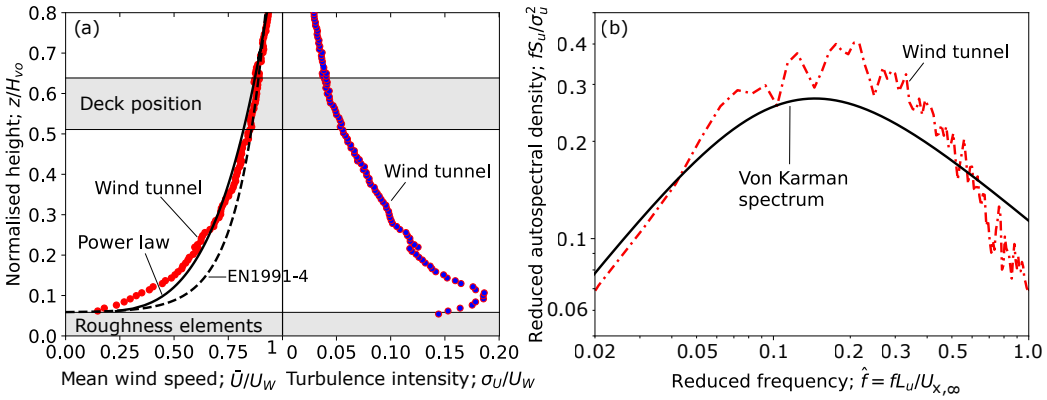

Figure 8: Stream-wise wind flow properties in the WT without deck model: (a) mean wind speed and turbulence intensity profiles, (b) frequency spectrum of the wind velocity record at the height $z = 0.58H_{vo}$, normalised with respect to the mean speed at the same point ($U_{x,\infty}$).

The frequency content of the stream-wise turbulence measured at the height corresponding to the centroid of the vehicle model ($z = 0.58H_{vo}$) is consistent with the corresponding Von Karman spectrum shown in Fig. 8(b), which is described as

$$\frac{fS_u}{\sigma_u^2} = \frac{4\hat{f}_u}{\left(1 + 70.8\hat{f}_u^2\right)^{5/6}}, \tag{3}$$

where S_u and σ_u are the auto-spectral density and the standard deviation of the turbulent component, f is the frequency and $\hat{f}_u = fL_u/U_{x,\infty}$ its reduced expression. It refers to the recorded flow velocity at the level of deck in the

study of the wind field of the empty tunnel, for which the mean wind speed is $U_{x,\infty} = 7.9$ m/s, and the along-flow turbulence length-scale is measured as $L_u = 0.84$ m.

The dimensions of the typical deck cross-section tested in the WT are included in Fig. 2(b), with $d = 85$ mm to give a scale factor of 1/50 with respect to the midspan segment of the Orwell Bridge deck. In order to inform the design of the tunnel setup, a series of 3D CFD simulations were conducted in OpenFOAM [38] using the same numerical scheme described previously. The simulations showed that even with a relatively long deck of 2.4 m the wake of the upwind edge under the most inclined wind tested ($\alpha = 45°$) affected the vehicle located at its centre, particularly in Lane 4 (downwind) as shown in Fig. 9(a). Therefore, it was decided to place the vehicle at the quarter-span of the deck, 0.6 m away from its downwind end, where such effect is reduced (Fig. 9(b)). Three different end plates were built in plywood to adjust to the upwind end of the deck model at skew wind angles of $\alpha = 45°$, 60° and 75°. In order to prevent clashing with the road furniture a small gap was left between the edge barriers and the plate, and it was covered by a small flexible screen to avoid the wind flow through the plate. The CFD results showed that the plate was not needed at the downwind end of the deck to explore the wind flow around the vehicle. The influence of the upwind end plate in the experimental results is considered further in Section 4.4. Regardless of the use of end plates, the CFD analysis also suggested that very skew incidence angles, with $\alpha < 45°$ (or $\alpha > 135°$) cannot be tested accurately in the current setup because the flow disturbances originated at the upwind end of the deck propagate to the vehicle.

The stiff timber deck model includes all the relevant details of the parapets and barriers with a tolerance of $\pm$ 1 mm. The bridge model was mounted on the tunnel's turntable using two vertical metal struts bolted to the underside of the model. These props have a small cross-section to minimise the obstruction to the wind flow because they are only used to hold the deck with vehicles at a height of approximately 600 - 800 mm from the tunnel's floor, and not to represent the actual piers of the bridge. The blockage ratio of the model in the WT is approximately 6%. Fig. 10 shows the test setup.

The WT is operated with an incoming wind speed at the level of the deck of $U_{x,\infty} \approx 8$ m/s, resulting in a Reynolds number Re $\approx 2.5 \times 10^5$. This is lower than the expected Re numbers in actual bridges, but it has a small effect in the results according to other WT studies on scaled vehicle-bridge models that reached Re values in the same order of magnitude (e.g. [25, 43, 44]).

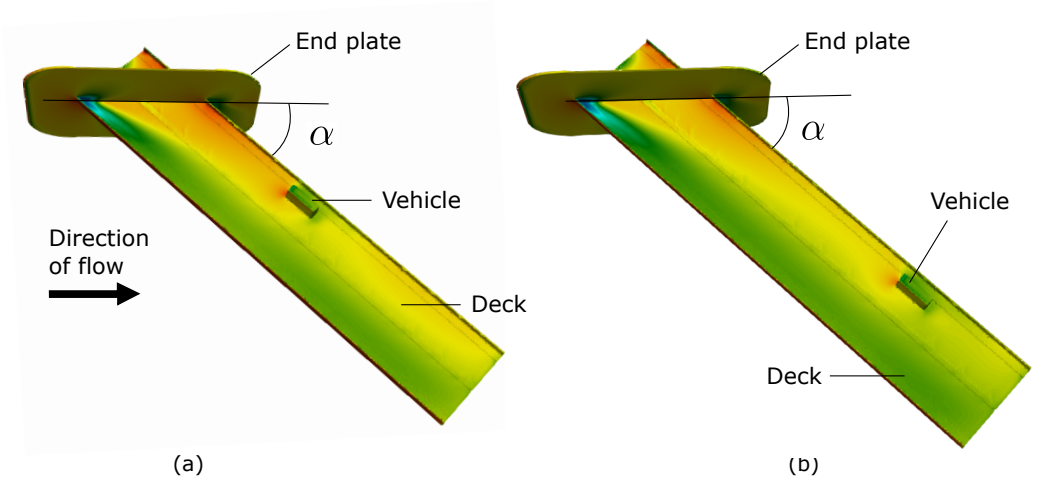

Figure 9: Normalised pressure contour map in the 2.4-m long deck model with an idealised vehicle on the leeward lane: (a) vehicle at midspan, (b) vehicle at downwind quarter-span. Both cases consider skew wind with $\alpha = 45°$, going from left to right. The red and blue colour indicates the regions with highest and lowest pressures.

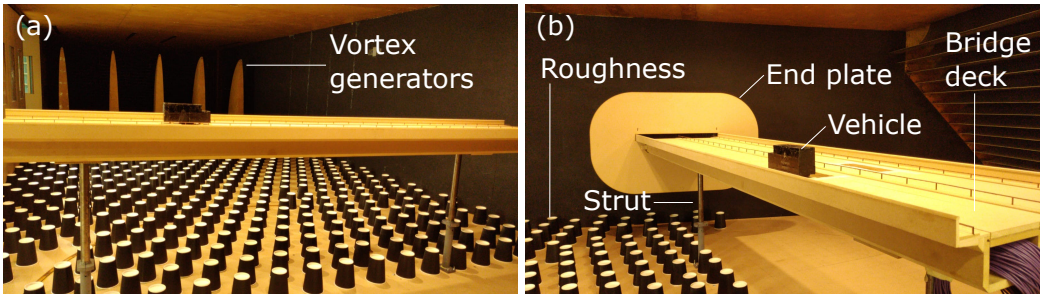

Figure 10: Setup of the model in the WT: (a) view of the model with the vortex generators behind, (b) view of the deck cross-section with the pressure tap tubes going to the vehicle, and the plate at the upwind end of the deck.

4.2. Vehicle model

The vehicle in this study is a 1/50-scale model of a typical rigid truck with a simplified shape to facilitate manufacturing and maintain generality in the results. The dimensions of the vehicle are included in Fig. 11(a), along with its reference local axes (x_v, y_v, z_v) and the position of its centroid. This point is not the actual centroid of the physical model of the vehicle, but it represents a conventional location of the centroid of unladen rigid trucks reported in literature [16, 45]. The wheels are simplifed as 6-mm thick timber segments that represent the equivalent blockage of typical wheels to cross winds. A 64-channels pressure scanner is used to calculate the aerodynamic actions on the vehicle.

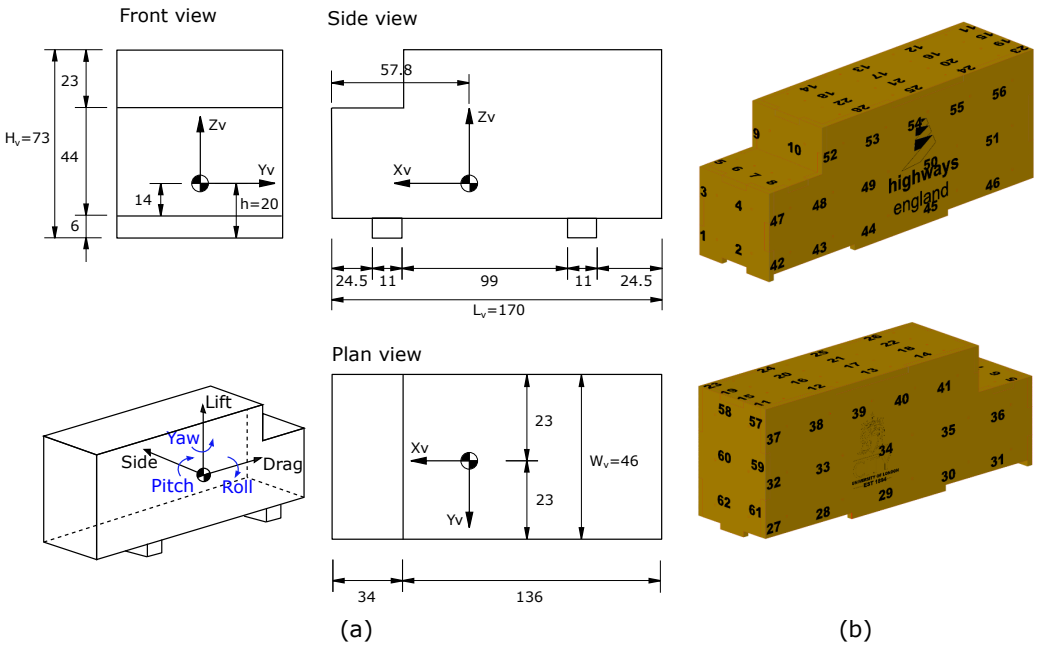

Figure 11: High-sided vehicle model used in the WT testing: (a) views with dimensions in mm, (b) distribution of pressure taps.

The vehicle model is made of acrylic plastic elements that are interlocked and glued together to form all its faces. They have a total of 62 pressure taps that were laser-cut. The distribution of these sensors in the vehicle is designed to capture the pressure gradients for different wind incidence angles, using as a reference the pressure maps obtained from the 3D CFD. The distribution and the numbering of the pressure taps on the faces of the

vehicle is included in Fig. 11(b). The wheels of the vehicle are screwed to a sliding plate that fits in the upper slab of the deck model. It allows the vehicle to be placed on the centreline of the road lanes (L1 - L4) of the deck. The tubes that connect the pressure taps on the vehicle with the pressure scanner are mounted inside the hollow deck girders to avoid interference with the air flow. It is noted that the lift forces on the vehicle are not obtained because of the lack of pressure taps at its bottom face.

The side and drag forces (F_S and F_D), as well as the rolling, pitching and yawing moments (M_R, M_P and M_Y) are calculated at every instant from the time-history recording of the pressure at each of the $N_t = 62$ taps shown in Fig. 11(b):

$$F_S(t) = \sum_{i=1}^{N_t} P_i(t) A_i n_i^{y_v} \tag{4a}$$

$$F_D(t) = \sum_{i=1}^{N_t} P_i(t) A_i n_i^{x_v} \tag{4b}$$

$$M_R(t) = \sum_{i=1}^{N_t} P_i(t) A_i n_i^{y_v} (z_i - z_G) + P_i(t) A_i n_i^{z_v} (y_i - y_G) \tag{4c}$$

$$M_P(t) = \sum_{i=1}^{N_t} P_i(t) A_i n_i^{z_v} (x_i - x_G) + P_i(t) A_i n_i^{x_v} (z_i - z_G) \tag{4d}$$

$$M_Y(t) = \sum_{i=1}^{N_t} P_i(t) A_i n_i^{y_v} (x_i - x_G) + P_i(t) A_i n_i^{x_v} (y_i - y_G), \tag{4e}$$

where $P_i(t)$ and A_i are the instantaneous pressure and contributing area of the i-th tap; $(n_i^{x_v}, n_i^{y_v}, n_i^{z_v})$ are the three components of the vector normal to the surface of the vehicle at the pressure tap i, in the Cartesian coordinate system of the vehicle (x_v, y_v, z_v) shown in Fig. 11(a); (x_i, y_i, z_i) are the coordinates of the i-th pressure tap in these axes; and (x_G, y_G, z_G) are the local coordinates of the centroid of the vehicle, which are (0,0,0) in this case because it coincides with the origin of the vehicle coordinate system. The convention for positive pressures is that they point inside the vehicle, and the positive normal vector at the surfaces also points inside the volume of the vehicle. During the WT testing the instantaneous pressure $P_i(t)$ is recorded for 180 s with an adquisition frequency of 10 Hz.

We obtained the time-averaged aerodynamic coefficients from the time-history results given in Eq. (4). The quasi-steady force coefficients are

$$C_j = \frac{F_j}{0.5\rho U_{x,\infty}^2 A_f}, \tag{5}$$

with the subindex $j = S, D$ refering to the side and drag forces, respectively. $A_f = 3082$ mm^2 is the area of the back face of the vehicle, and $\rho \approx 1.2$ kg/m^3 is the density of the air measured during the experiment. Similarly, the quasi-steady moment coefficients are

$$C_j = \frac{M_j}{0.5\rho U_{x,\infty}^2 A_f h}, \tag{6}$$

in which $j = R, P, Y$ represent the rolling, pitching and yawing moments, respectively, and $h = 20$ mm is the vertical distance from the wheel/deck interface and the centroid of the vehicle (Fig. 11(a)).

4.3. Test programme

The experimental programme aims to cover a wide range of combinations of the wind incidence angle (α) and the position of the vehicle across the width of the deck, which is always centered on one of the four road lanes shown in Fig. 2(b). To facilitate the comparison of the results, the vehicle is orientated southbound (with the local vehicle axis x_v pointing at the bottom) regardless of the lane occupied and the wind incidence angle, as it is illustrated in Figs. 12(a) and (b). The incidence angles range from $\alpha = 45°$ to $\alpha = 135°$, with an interval of 5°. As it was observed in the CFD simulation, if the wind incidence angle is between $\alpha = 45°$ and $\alpha = 90°$ the upwind side of the deck model (which is the northbound one in Fig. 12(a)) does not affect the wind flow around the vehicle. However, when $\alpha > 90°$ the upwind end of the deck becomes the southbound one, and the test would require to move the end plate and the vehicle to the opposite side of the bridge, or to disassemble the whole bridge and rotate it 180° to reach the setup in Fig. 12(b). Symmetry is exploited to avoid this difficulty, and the vehicle is rotated to face to the northbound end of the deck for the tests with $\alpha > 90°$. This leads to the configuration described in Fig. 12(c), which is equivalent to Fig. 12(b) with $\alpha = \alpha^* + 90°$, and α^* being the apparent wind incidence angle in the test with x_v northbound. Hereinafter, no mention is made to the orientation of the vehicle in the test and only the wind incidence angle α is reported.

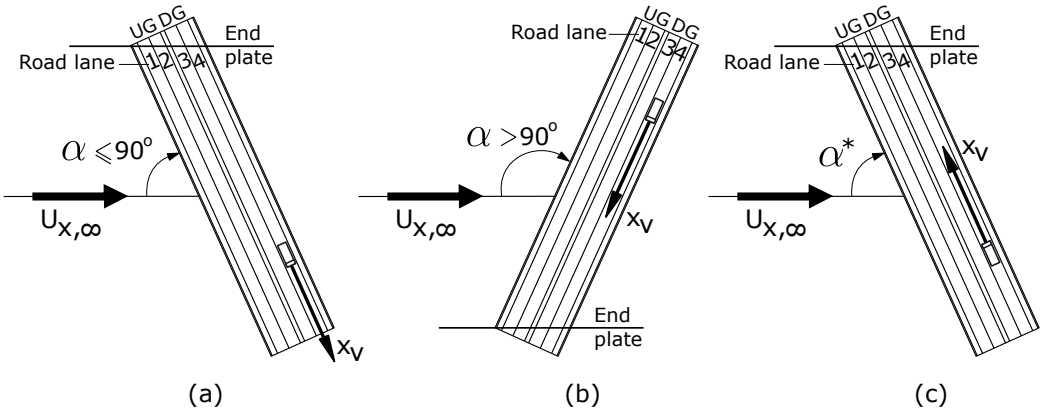

Figure 12: Plan view of the test configurations (looking from above) with wind incidence angles: (a) $\alpha \leq 90°$, (b) $\alpha > 90°$, and (c) $\alpha > 90°$ with opposite vehicle orientation (x_v) to make it equivalent to (b). Note that the vehicle is static during testing. UG and DG refer to the upwind and downwind girders of the bridge, respectively.

In total, 76 different wind-vehicle configurations have been tested without end plates, and 24 additional cases are repeated with these elements for angles $\alpha = 45°$, $60°$, $75°$, $105°$, $120°$ and $135°$ to explore their influence in the results.

4.4. Results of the wind tunnel testing

The time-averaged pressure ($\bar{P}_i$) measured on the faces of the vehicle when it occupies different lanes and it is subject to purely cross wind ($\alpha = 90°$) is presented in Fig. 13. The tributary area of each tap is coloured according to its pressure, intentionally avoiding the use of smoothing interpolators to show the actual test data. Regardless of the lane occupied by the vehicle, the results in Fig. 13 show negative pressure (suction) in all its faces apart from the windward side when $\alpha = 90°$, and this is because of the separation of the flow around the sharp corners of the vehicle faces. On the other hand, the windward side of the vehicle presents a characteristic gradient of pressures that goes from negative at the bottom to positive at the top due to the diversion of the wind flow exerted by the upwind edge barrier of the deck. This effect increases the rolling moment and it is most significant when the vehicle is closer to the barrier (lane 1), reducing its importance as the vehicle moves to the downwind edge. In order to visualise the flow, a stream of smoke was introduced upstream of the deck, at the level of its barrier. Fig. 14 shows two frames of the visualised smoke, which indicate that the flow is diverted by the barrier and thereafter impacts the top of the vehicle.

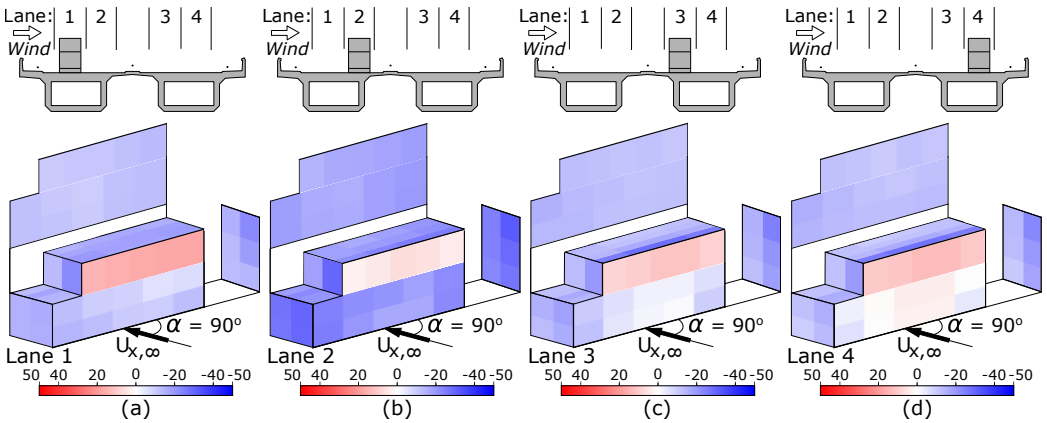

Figure 13: Time-averaged pressure distribution on the vehicle located in: (a) lane 1, (b) lane 2, (c) lane 3, and (d) lane 4. Purely cross wind $\alpha = 90°$. The red and the blue colours indicate positive and negative pressures, respectively. Units in Pa.

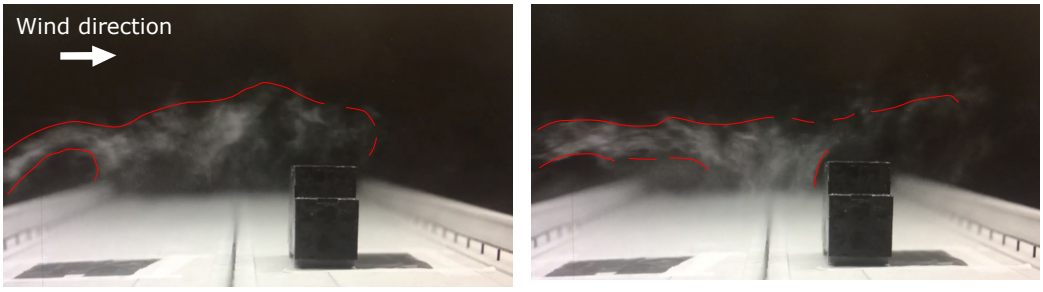

Figure 14: Two frames of the smoke flow recorded by a high-speed camera in the WT testing of the typical bridge, with the vehicle located on lane 3. Purely cross wind ($\alpha = 90°$) going from left to right.

The wind flow and the pressure distribution on the vehicle changes significantly with the incidence angle, as illustrated in Figs. 15 and 16 for skew wind angles with $\alpha = 45°$ and $\alpha = 135°$, respectively (without end plate). This is particularly true in the downwind lanes and it is attributed to (1) the flow reattachment in this part of the deck due to the increased along-wind width of the deck for skew incidence angles, and (2) the flow channelling effects discussed previously. The latter affects the vehicle as a combination of flow diversion (γ) within the height of the parapets (plane P1, see Fig. 6(a)), and the increment in the velocity magnitude (U_h) in the full height of the vehicle (planes P1 and P2, Fig 7(a)). With $\alpha = 45°$ and $\alpha = 135°$, the shielding effect of the edge parapet is only visible in the windward side face of the vehicle located on the upwind girder (lanes 1 and 2). When it is on the downwind girder (lanes 3 and 4) most of this face is under positive pressure, with an along-deck gradient that contributes to the yawing moment in the vehicle. This effect is also present in the suction measured on the leeward face of the vehicle, which contrasts with the approximately uniform suction observed on this face under cross-winds, as seen in Fig. 13.

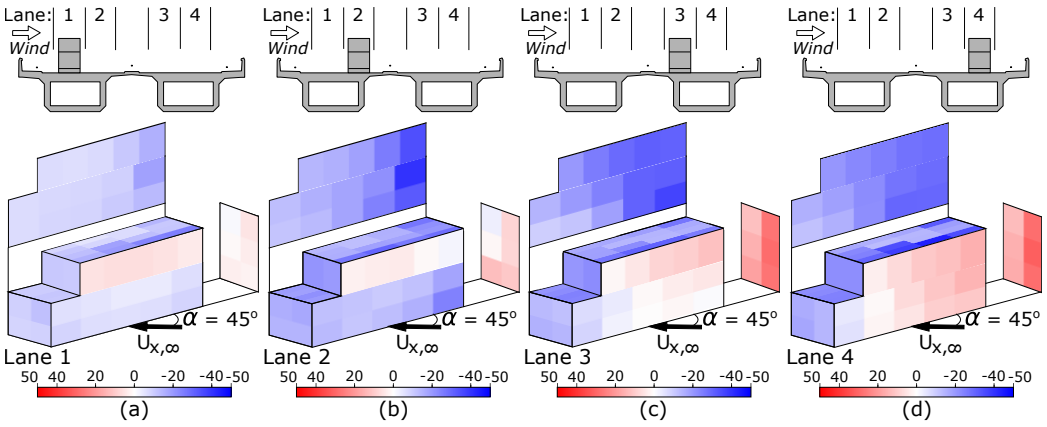

Figure 15: Time-averaged pressure distribution on the vehicle located in: (a) lane 1, (b) lane 2, (c) lane 3, and (d) lane 4. Skew wind $\alpha = 45°$. The red and the blue colours indicate positive and negative pressures, respectively. Units in Pa.

The skew wind angles $\alpha = 45°$ and $\alpha = 135°$ fall within the full-channelling Zone III identified in the CFD analysis of Section 3, and its characteristic along-deck diversion of the flow contribute to the vehicle pressure maps recorded in Figs. 15 and 16. Under very skew tail-winds ($\alpha = 45°$) the pressure at the rear face of the vehicle is higher than at its windward side, which

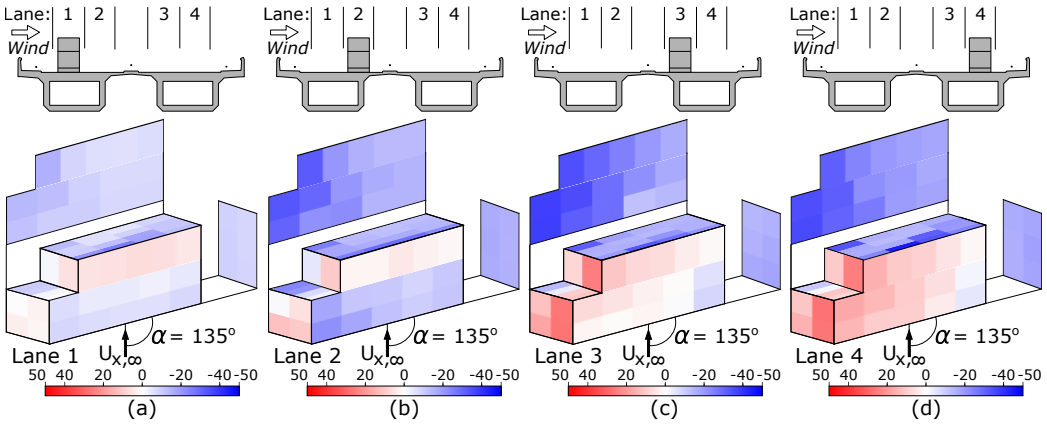

Figure 16: Time-averaged pressure distribution on the vehicle located in: (a) lane 1, (b) lane 2, (c) lane 3, and (d) lane 4. Skew wind $\alpha = 135°$. The red and the blue colours indicate positive and negative pressures, respectively. Units in Pa.

affects the vehicle drag and it is attributed to the along-deck wind flow on the deck, particularly in lanes 3 and 4 (Figs. 15(c) and (d)). The same effect is observed in the case with skew head-wind $\alpha = 135°$, but in this case the large positive pressure is recorded at the front vehicle face (Figs. 16(c) and (d)). We also note that the increment of suction at the windward edge of the vehicle top for very skew winds was also reported by [46] testing a similar vehicle in an open flat surface (off-bridge), which suggests that it is due to the wind incidence angle and not to the wake of the parapets.

Following the study of the pressure distribution on the vehicle, the discussion now focuses on the resultant wind effects. Fig. 17 presents the side coefficient (C_S) of the vehicle located in both girders, and compares it with the off-bridge coefficient given by Baker [16] to highlight the important differences with the on-bridge aerodynamic effects for a wide range of wind incidence angles. The zonification of skew winds observed in the CFD analysis of Section 3 is also included, which is proven to have an important effect in the results obtained experimentally. The side coefficient for winds in Zone I (small incidence angles) is reduced by approximately 42%, 83%, 66% and 53% in lanes 1, 2, 3 and 4, respectively, with respect to the corresponding off-bridge reference value. This indicates that the shielding of the upwind edge barrier reduces the side force significantly for purely or nearly-cross winds, especially in lane 2 because it is where the region of low wind speeds across the deck (referred to as 'protective bubble') created by the windward

barrier is higher. However, this effect diminishes as the vehicle moves to the downwind lanes. On the other hand, the side force is reduced by increasing the wind incidence angle in the transition Zone II when the vehicle is in lane 1, but it is almost insensitive to changes of α within this Zone when the vehicle is in other lanes. The picture changes significantly under large skew wind angles in Zone III, where the side force on the vehicle increases with α in Zone III for all the road lanes, but particularly in the downwind girder lanes 3 and 4 (Fig. 17(b)), for which C_S rises by up to 80% when α varies only 25% (from 60° to 45°). This is attributed to the reattachment of the wind flow on the downwind girder for very skew wind angles in Zone III.

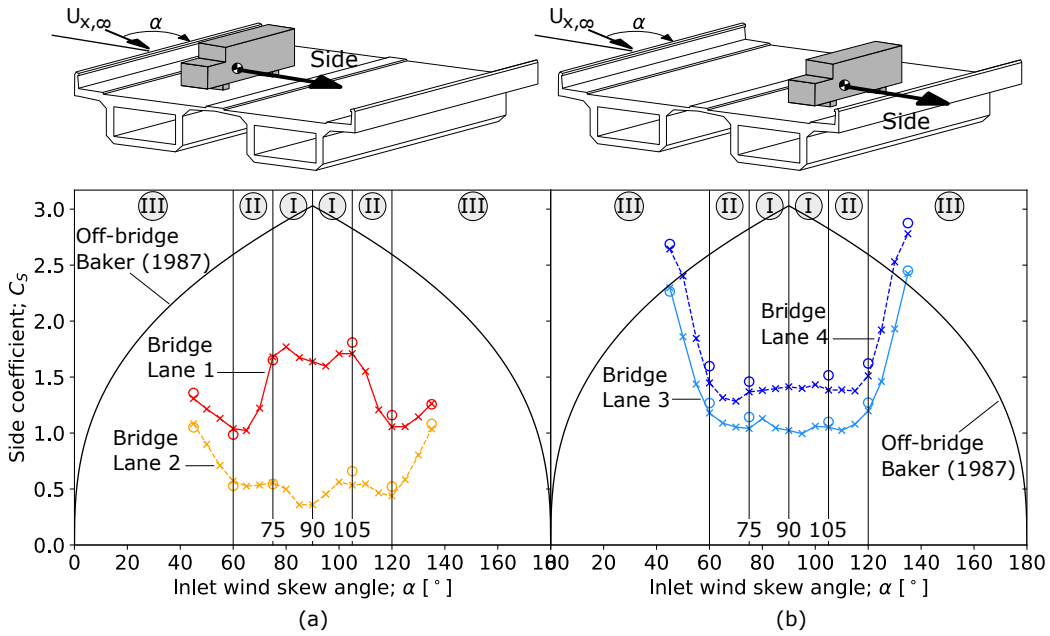

Figure 17: Side coefficient of the vehicle in: (a) upwind girder, and (b) downwind girder. The off-bridge side coefficient given by Baker [16] is included for comparison. The cross markers connected with lines refer to the tests without end plate, whilst the circular markers indicate the results with end plate. The positive convention for side forces in the vehicle is included.

The drag coefficient (C_D) is included in Fig. 18, and it also shows its dependency with the skew wind zonification and the position of the vehicle across the width of the deck. The drag increases more with α in Zone I than in Zone II, which can be connected with the smaller change of the inclination angle of the horizontal wind along the deck (γ) in Zone II, as it was described

in Fig. 5(a). However, when the wind flow is fully channelled in Zone III the drag coefficient grows at a higher rate with the wind incidence angle. This is observed in all the lanes, but the influence of α is stronger in the downwind girder (Fig. 18(b)) resulting in drag coefficients in lanes 3-4 that are larger than those in lanes 1-2, also exceeding the reference values for the vehicle in open terrain. This is explained by the large wind pressure in the rear or front vehicle faces for tail- or head-winds, respectively, as shown in Figs. 15(c)-(d) and 16(c)-(d), which is attributed to the flow channelling in Zone III.

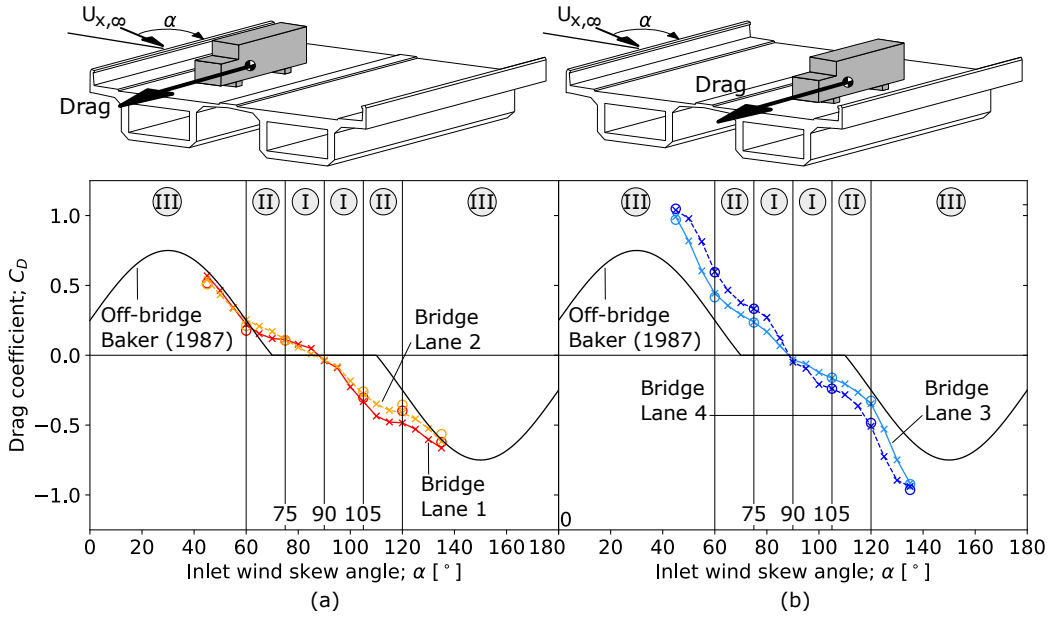

Figure 18: Drag coefficient of the vehicle in: (a) upwind girder, and (b) downwind girder. The off-bridge side coefficient given by Baker [16] is included for comparison. The cross markers connected with lines refer to the tests without end plate, whilst the circular markers indicate the results with end plate. The positive convention for drag forces in the vehicle is included.

Fig. 19 shows that the influence of the wind incidence angle α on the rolling moment of the vehicle (C_R) is closely related to that on the side force. The exception is mainly in Lane 1 for highly skew winds, in Zone III, where the rolling coefficient is strongly reduced. This is because the vertical pressure gradient observed in the windward vehicle face for cross-winds gives way to a more uniform pressure distribution in the vertical direction when $\alpha < 60°$ (Fig. 15(a)) or $\alpha > 120°$ (Fig. 16(a)). However, the same range of skew angles in Zone III increases the rolling moment in the downwind girder even

beyond the off-bridge reference value (Fig. 19(b)), both for tail- and head-winds. This may be due to the larger positive and negative pressures recorded at the top of the vehicle's windward and leeward side faces, respectively, when it is in lanes 3 and 4 and the incidence angle of the wind is in Zone III (see Figs. 15(c)-(d) and 16(c)-(d)), in combination with the relatively low position of the centroid of the vehicle.

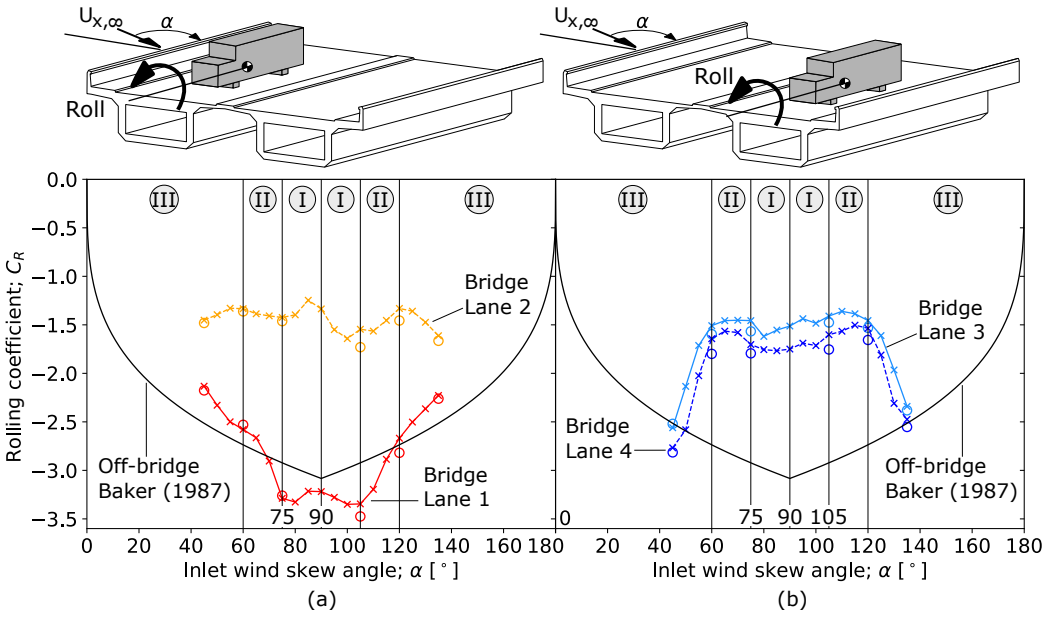

Figure 19: Rolling coefficient of the vehicle in: (a) upwind girder, and (b) downwind girder. The off-bridge side coefficient given by Baker [16] is included for comparison. The cross markers connected with lines refer to the tests without end plate, whilst the circular markers indicate the results with end plate. The positive convention for rolling moments in the vehicle is included.

The pitching and the yawing moment coefficients of the vehicle (C_P and C_Y) are included in Figs. 20 and 21, respectively. The apparent asymmetry of these two actions with respect to the cross-wind angle of incidence $\alpha = 90°$ contrasts with the other aerodynamic coefficients, particularly due to the large increments of C_P and C_Y for Zone III head-winds ($\alpha > 120°$) in lanes 1 and 2, and for tail-winds ($\alpha < 60°$) in lanes 3 and 4. The pitching moment is larger than the off-bridge vehicle reference value in the upwind girder, especially in lane 1, when $\alpha > 120°$ (Fig. 20(a)). This is attributed to the pressure imbalance at the top vehicle face shown in Figs. 15 and 16, and it also appears on its side faces (windward and leeward) to contribute

to the yawing moment presented in Fig. 21. Lane 1 shows values of C_Y that are similar to those in the off-bridge vehicle for all the angles tested apart from skew headwinds with $\alpha > 120°$ that fall in Zone III, for which the yawing moment increases significantly. The same happens in Lane 2, which is significantly shielded until $\alpha > 120°$. The effect is more significant in the downwind girder, in which the yawing moment is relatively low for angles in Zones I and II, but increases significantly in Zone III, particularly for tailwinds with $\alpha < 60°$. Indeed, when $\alpha = 45°$ the value of C_Y is more than 5 times higher than with $\alpha > 60°$. This is explained by the horizontal pressure gradient increasing towards the windward face of the vehicle for very skew tailwinds when it is in the downwind girder, favoured by the flow channelling in Zone III as depicted in Figs. 15(c) and (d). The effect is stronger under tailwinds because the distance between the centroid of the vehicle and its rear side is larger than to its front side (Fig. 11(a)).

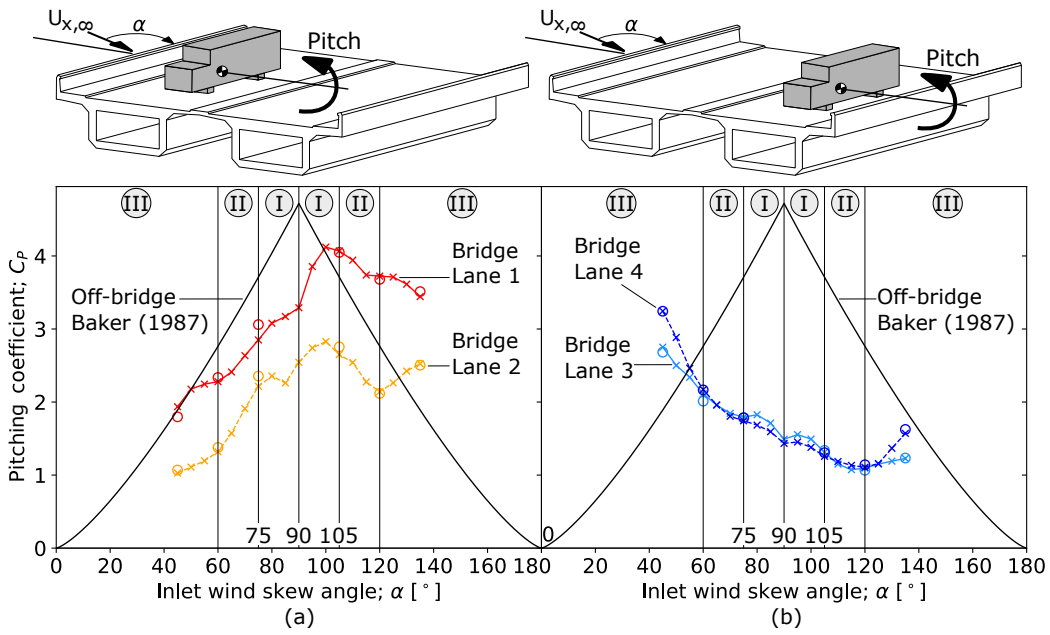

Figure 20: Pitching coefficient of the vehicle in: (a) upwind girder, and (b) downwind girder. The off-bridge side coefficient given by Baker [16] is included for comparison. The cross markers connected with lines refer to the tests without end plate, whilst the circular markers indicate the results with end plate. The positive convention for pitching moments in the vehicle is included.

It is observed in Figs. 17 - 21 that the results with the end plate installed

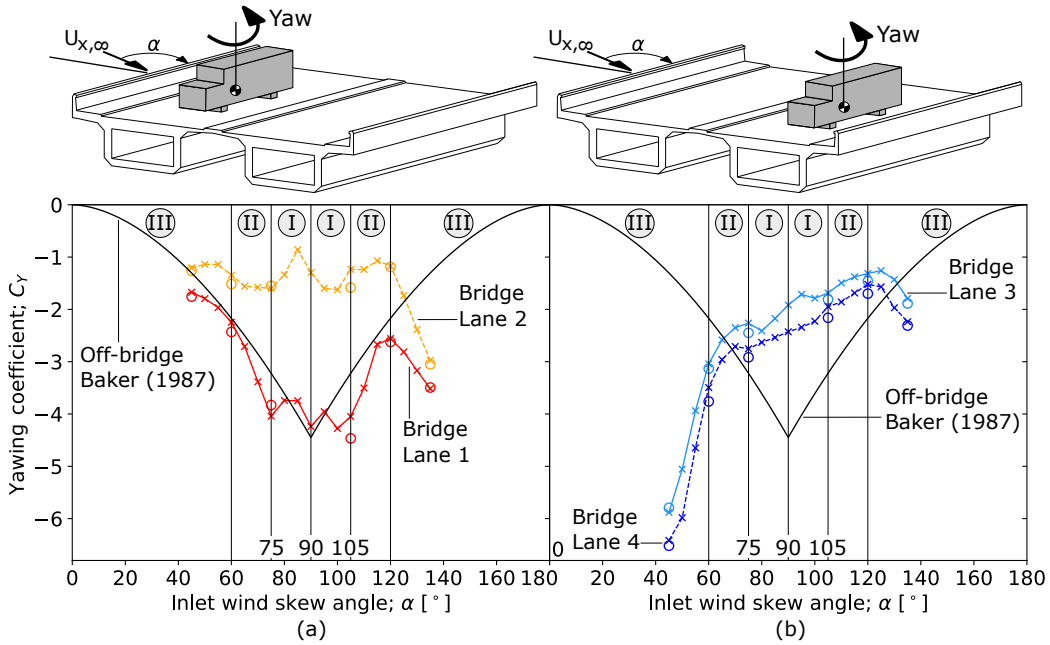

Figure 21: Yawing coefficient of the vehicle in: (a) upwind girder, and (b) downwind girder. The off-bridge side coefficient given by Baker [16] is included for comparison. The cross markers connected with lines refer to the tests without end plate, whilst the circular markers indicate the results with end plate. The positive convention for yawing moments in the vehicle is included.

in the bridge model are very similar to the corresponding cases without this element, with a maximum difference in the order of 10%. This indicates that under non-orthogonal winds the upwind end of the model does not affect significantly the flow around the vehicle thanks to the length of the deck model, and it validates the use of the results without end plate for all the wind incidence angles tested. In the following, the WT test results correspond to cases without this element.

4.5. Further considerations on wind channelling effects

The along-deck channelling of the wind field is explored further considering the horizontal vehicle aerodynamic force vector that results from the combination of the side and the drag forces in the horizontal plane $(x-z)$, as shown in Fig. 1(c). The magnitude of this vector, $F_{SD} = \sqrt{F_S^2 + F_D^2}$, is normalised with respect to the projected area of the vehicle in the wind direction:

$$C_{SD} = \frac{F_{SD}}{0.5\rho U_{x,\infty}^2 L_p H_v}, \tag{7}$$

this is to avoid distorting the results because the area of the vehicle's side face is larger than the rear one. In Eq. (7) $H_v = 73$ mm is the height of the vehicle and L_p is the projected length of the vehicle plan in the wind direction: $L_p = L_v \sin(\alpha) + W_v \cos(\alpha)$, with $L_v = 170$ mm and $W_v = 46$ mm being the length and the width of the vehicle, respectively (see Fig. 11(a)).

The results of the combined side-drag coefficient are obtained in each time frame during testing and their average values are presented in Fig. 22. The horizontal force exerted by the wind on the vehicle is almost insensitive to changes in the wind incidence angle when it is moderately skewed, in Zones I and II, for all the lanes with the exception of the upwind one (lane 1). However, the transition to Zone III marks a strong increment of the horizontal wind force as it becomes more inclined with respect to the deck, particularly in lanes 3-4 as shown in Fig. 22(b). This is attributed to the along-deck channelling of the wind field within the height of the barriers, combined with flow reattachment in the downwind girder.

The angle ψ between the horizontal aerodynamic force on the vehicle and the inlet wind direction that was described in Fig. 1(c) is:

$$\psi = \arctan\left[\frac{F_D \cos(\alpha) + F_S \sin(\alpha)}{F_D \sin(\alpha) - F_S \cos(\alpha)}\right], \tag{8}$$

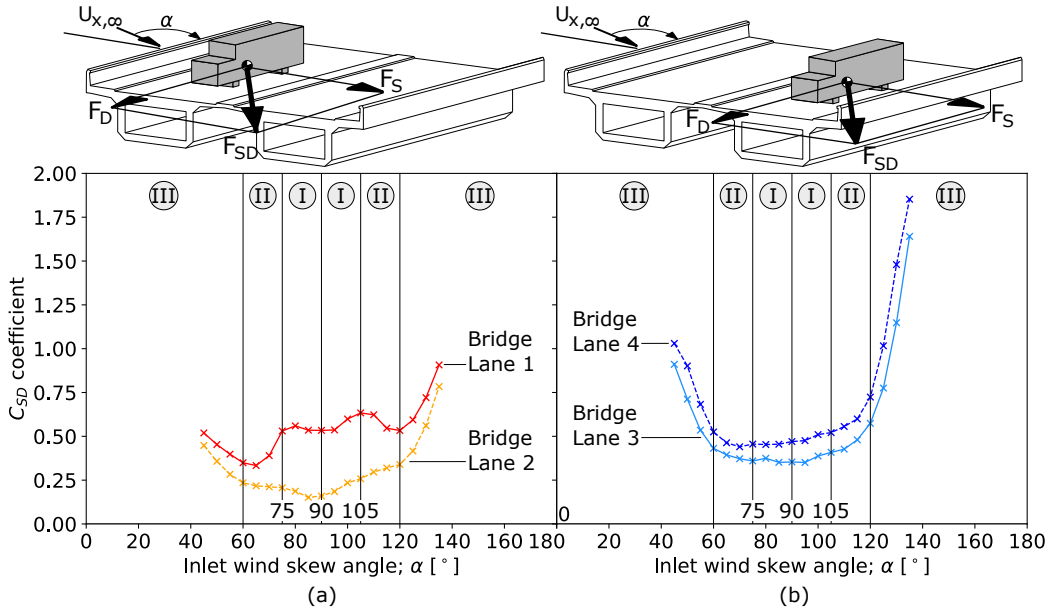

Figure 22: Combined side-drag aerodynamic coefficient C_{SD} of the vehicle in (a) upwind girder, and (b) downwind girder. The positive convention for side and drag forces in the vehicle is included.

which is averaged in Fig. 23 from the instantaneous values measured in the WT. The results indicate that the deviation of the side-drag force resultant with respect to the wind incidence angle is relatively small (within $\psi \pm 10°$) in Zones I and II, with the exception once again of Lane 1 and $\alpha < 75°$ due to the large wind exposure in this part of the deck. The small value of ψ in Zones I and II indicates that for moderate-to-low wind incidence angles the horizontal force F_{SD} on the vehicle is almost aligned with the inlet wind direction. However, large deviations between the direction of wind and F_{SD} appear in Zone III due to the flow channelling along the deck, particularly in the downwind girder.

However, there are significant differences between the angle ψ measured in the WT and the direction of wind within the height of the barriers (γ), because the former is affected by the aerodynamic pressure on the vehicle above the barriers. For this reason additional WT tests with light-weight woolen tufts distributed along the centre of the four lanes were conducted to visualise the orientation of the wind flow along the deck, close to the pavement surface. One end of these tufts was fixed to the model and they

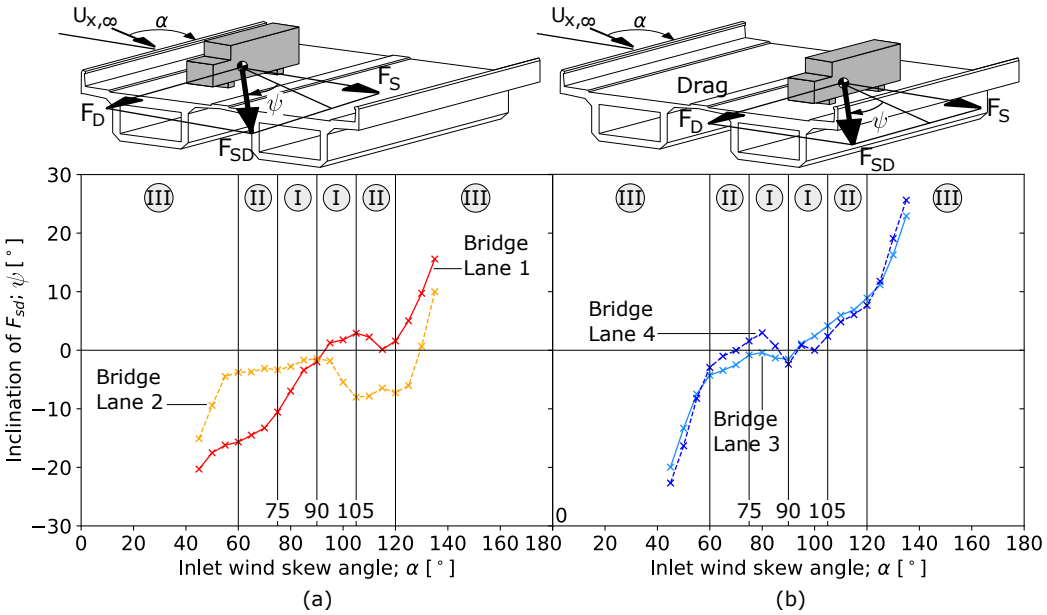

Figure 23: Angle ψ between the inlet mean wind speed direction and the horizontal side-drag resultant force F_{SD} in (a) upwind girder, and (b) downwind girder. The positive convention for the angle ψ is included.

are shown as black lines in the plan views of the testing included in Fig. 24, where the numbers 1, 2, 3 and 4 refer to the corresponding road lanes. During testing, a high-speed camera mounted above the model was used to study the movement of the tufts. The orientation of the wind flow at the pavement level, γ (Fig. 1(b)), was estimated by identifying which tufts were actively moving during the tests and averaging the angle that they formed with the horizontal line. The lines in Fig. 25 show the angle of wind along the deck, after averaging separately the values of γ in the active wool strips of the lanes in the two girders. The figure also includes shaded bands that represent one standard deviation of γ above and below the mean value.

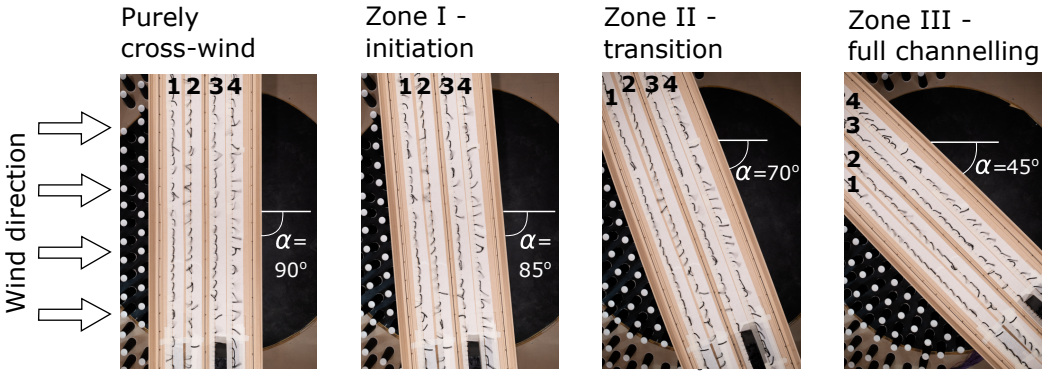

Figure 24: Plan view of the experimental measurement of the along-deck wind inclination (γ) in the WT for wind incidence angles (α) that are representative of different flow regions.

The experimental results in Fig. 25 are compared with those obtained from the CFD analysis of the wind flow within the height of the barriers (Plane 1) in the generic bridge deck discussed in Section 3. The results of both studies are consistent, even though the experimental testing and the CFD results refer to slightly different deck cross-sections (see Fig. 2). The differences between CFD and WT testing are higher for wind flows that are fully or nearly perpendicular to the deck, because the larger shielding effect of the barriers reduces significantly the mean wind speed close to the pavement level (also observed in the CFD results of Fig. 5(b)-(c)), and the movement of the tufts is more chaotic as it can be observed in the large standard deviation of the angle γ across the deck in Zone I. However, the influence of the skew angle α on the wind flow in the downwind region of the deck agrees well with the three different zones described in the CFD study. As it was observed in the numerical analysis, the WT testing shows that γ is smaller than α

in the downwind girder. The larger differences between the inclination of the wind flow in the upwind girder of the tested bridge, compared with the CFD results, are attributed to a stronger recirculation effect, observed in the inclination of the tufts in lanes 1 and 2 in Fig. 24. Nevertheless, for very large skew angles in Zone III the experimental results indicate that the flow in these lanes is almost aligned with the deck, resulting in a fully channelled flow.

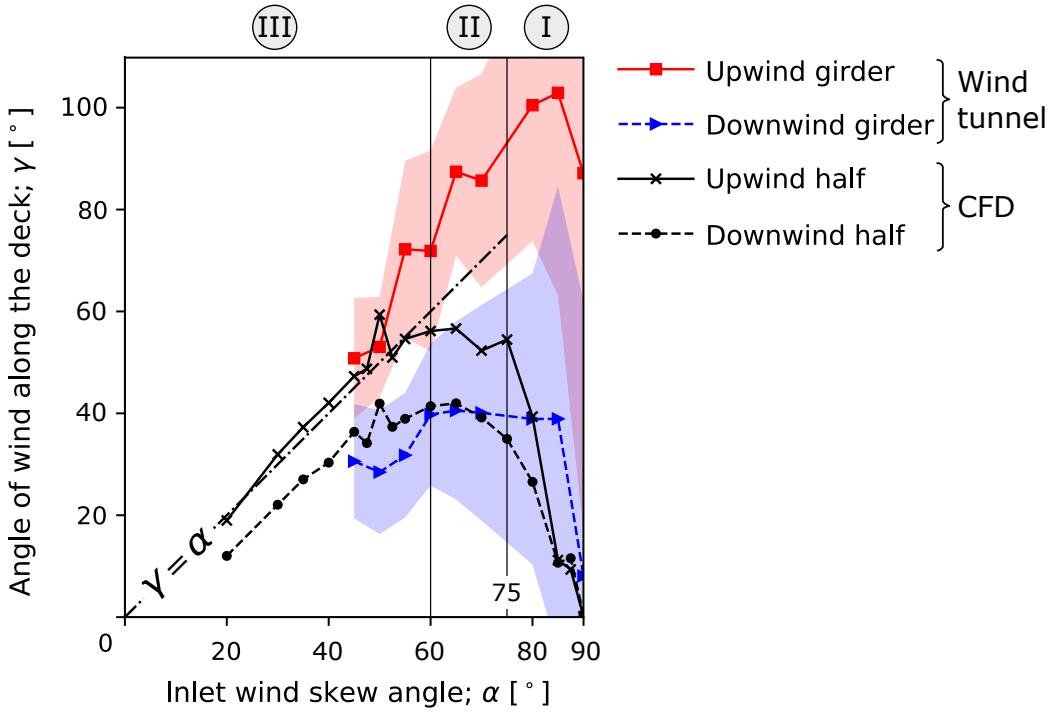

Figure 25: Comparison of the along-deck wind inclination (γ) obtained with WT testing in the typical bridge, and with CFD in Plane P1 of the generic bridge.

5. Conclusions

This work studied the effect of the angle of incidence of the wind on the flow around bridge decks with low-rise edge parapets ($h_f/d = 1/3$), and how it affects the aerodynamic forces and moments on vehicles. To this end, a generic (idealised) deck model with different barrier configurations is studied using computational fluid dynamic (CFD) analysis. The work continues with

an extensive wind tunnel (WT) testing programme on a deck model that represents a real bridge with a conventional configuration of relatively short side barriers. The following conclusions are drawn:

- The CFD analysis of the generic deck model showed that a low-rise windward edge parapet is able to introduce a significant diversion of the wind velocity field along the deck for skew incidence angles. This flow diversion mainly occurs within the height of the barriers.

- The effect of the wind skew angle (α) on the horizontal angle of inclination of the wind velocity along the deck (γ) is studied experimentally and numerically. In the region of the deck within the height of the barriers both methods show that for small incidence angles ($75° < \alpha < 105°$) γ rapidly changes to get closer to α (Zone I - Initiation); for intermediate skew angles γ is relatively insensitive to α (Zone II - Transition); and for very skew winds ($\alpha < 60°$ or $\alpha > 120°$) the wind flow is almost aligned with the deck (Zone III - Full channelling). The deviation of the wind velocity field by the deck is negligible above the parapets, regardless of the skew angle.

- The pressure maps on the vehicle faces obtained in the WT testing indicate that under purely cross-winds the low-rise parapets are able to shield significantly high-sided vehicles across the width of the deck, particularly in its centre and towards the windward side. However, the parapets direct the wind to the top of the vehicle, increasing the rolling moment in the most upwind lane.

- The skew wind angle affects significantly the pressure distribution and the resultant aerodynamic coefficients on the vehicle, which exceed the reference off-bridge values if α is in Zone III due to the along-deck flow and its reattachment in the downwind girder.

One limitation of this work is that it considers the vehicle as static in the wind tunnel testing. However, its relevance lies in the observation of significant flow disturbances around conventional bridge decks with relatively short edge parapets, which are widely used for the safety of traffic but routinely ignored in the aerodynamic actions on vehicles. More importantly, it is demonstrated that the wind field around vehicles changes significantly with the incidence angle. This suggests that the widely spread use of aerodynamic vehicle coefficients calculated from numerical or experimental models

in which the vehicle is static are not entirely valid in further wind-vehicle-bridge interaction analyses. This is because as the vehicle moves in this type of studies the relative angle of incidence of wind changes (β in Fig. 1(a)), and this cannot be directly related to the angle α used in the test with a static vehicle, as it was also argued by [28, 29] in railway bridges. Therefore, additional WT testing with moving vehicles for different wind incidence angles is needed.

Acknowledgements

This work stems from the project "Driving stability in the Orwell Bridge under high winds", funded by Highways England. Their support is greatly appreciated. Note that the reported results are not necessarily representative of the actual conditions in the Orwell Bridge.

References

[1] B. Smith, C. Barker, Design of wind screens to bridges; experience and applications on major bridges, in: International Symposium on Advances in Bridge Aerodynamics, Copenhagen, 1998, pp. 289–298, a.A. Balkema.

[2] R. Pritchard, Wind effects on high sided vehicles, Journal of Institute of Highway Transportation 56 (1985) 22–25.

[3] S.-D. Kwon, D. Kim, S. Lee, H. Song, Design criteria of wind barriers for traffic. part 1: Wind barrier performance, Wind and Structures 14 (1) (2011) 55–70.

[4] T. Zhang, H. Xia, W. Guo, Analysis on running safety of train on bridge with wind barriers subjected to cross wind, Wind and Structures 17 (2) (2013) 203–225.

[5] X. He, Y. Zou, H. Wang, Y. Han, K. Shi, Aerodynamic characteristics of a trailing rail vehicles on viaduct based on still wind tunnel experiments, Journal of Wind Engineering and Industrial Aerodynamics 135 (2014) 22–33.

[6] W. Guo, H. Xia, R. Karoumi, T. Zhang, X. Li, Aerodynamic effect of wind barriers and running safety of trains on highspeed railway bridges under cross winds, Journal of Wind Engineering and Industrial Aerodynamics 20 (2) (2015) 213–236.

[7] C.-R. Chu, C.-Y. Chang, C.-J. Huang, T.-R. Wu, C.-Y. Wang, M.-Y. Liu, Wind break protection for road vehicles against crosswind, Journal of Wind Engineering and Industrial Aerodynamics 116 (2013) 61–69.

[8] Y. Han, S. Liu, J. Hu, C. Cai, J. Zhang, Z. Chen, Experimental study on aerodynamic derivatives of a bridge cross-section under different traffic flows, Journal of Wind Engineering and Industrial Aerodynamics 133 (2014) 250–262.

[9] N. Chen, Y. Li, B. Wang, Y. Su, H. Xiang, Effects of wind barrier on the safety of vehicles driven on bridges, Journal of Wind Engineering and Industrial Aerodynamics 143 (2015) 113–127.

[10] J. Zhang, M. Zhang, Y. Li, X. Huang, Z. Zheng, Aerodynamics of high-sided vehicles on truss girder considering sheltering effect by wind tunnel tests, The Baltic Journal of Road and Bridge Engineering 15 (2) (2020) 66–88.

[11] X. Lin, B. Lin, D. Xia, L. Lin, Z. Yuan, Effects of wind barriers on wind fields and vehicle stability on bridges, Atmosphere 13 (318) (2022) 1–11.

[12] R. Scanlan, Estimates of skew wind speeds for bridge flutter, Journal of Bridge Engineering 4 (2) (1999) 95–98.

[13] L. Zhu, Y. Xu, F. Zhang, H. Xiang, Tsing Ma bridge deck under skew winds - part I: aerodynamic coefficients, Journal of Wind Engineering and Industrial Aerodynamics 90 (2002) 781–805.

[14] L. Zhu, Y. Xu, H. Xiang, Tsing Ma bridge deck under skew winds - part II: flutter derivatives, Journal of Wind Engineering and Industrial Aerodynamics 90 (2002) 807–837.

[15] Y. Zhou, L. Sun, Effects of high winds on a long-span sea-crossing bridge based on structural health monitoring, Journal of Wind Engineering and Industrial Aerodynamics 174 (2018) 260–268.

[16] C. Baker, Measures to control vehicle movement at exposed sites during windy periods, Journal of Wind Engineering and Industrial Aerodynamics 25 (1987) 151–161.

[17] S. Kim, C. Yoo, H. Kim, Vulnerability assessment for the hazards of cross-winds when vehicles cross a bridge, Journal of Wind Engineering and Industrial Aerodynamics 156 (2016) 62–71.

[18] A. Camara, Vehicle-bridge interaction and driving accident risks under skew winds, Journal of Wind Engineering and Industrial Aerodynamics 214 (2021) 104672.

[19] Y. Xu, W. Guo, Dynamic analysis of coupled road vehicle and cable-stayed bridge systems under turbulent wind, Engineering Structures 25 (2003) 473–486.

[20] C. Cai, S. Chen, Framework of vehicle-bridge-wind dynamic analysis, Journal of Wind Engineering and Industrial Aerodynamics 92 (7/8) (2004) 579–607.

[21] S. Chen, C. Cai, Accident assessment of vehicles on long-span bridges in windy environments, Journal of Wind Engineering and Industrial Aerodynamics 92 (2004) 991–1024.

[22] A. Camara, I. Kavrakov, K. Nguyen, G. Morgenthal, Complete framework of wind-vehicle-bridge interaction with random road surfaces, Journal of Sound and Vibration 458 (2019) 197–217.

[23] Y. Han, C. Cai, S. Chen, X. He, Effects of aerodynamic parameters on the dynamic responses of road vehicles and bridges under cross winds, Journal of Wind Engineering and Industrial Aerodynamics 134 (2014) 78–95.

[24] F. Cheli, R. Corradi, D. Rocchi, G. Tomasini, E. Maestrini, Wind tunnel tests on train scale models to investigate the effect of infrastructure scenario, Journal of Wind Engineering and Industrial Aerodynamics 98 (2010) 353–362.

[25] F. Dorigatti, M. Sterling, D. Rocchi, M. Belloli, A. Quinn, C. Baker, E. Ozkan, Wind tunnel measurements of crosswind loads on high sided

vehicles over long span bridges, Journal of Wind Engineering and Industrial Aerodynamics 107-108 (2012) 214–224.

[26] F. Cheli, F. Ripamonti, E. Sabbioni, G. Tomasini, Wind tunnel tests on heavy road vehicles: Cross wind induced loads - part 2, Journal of Wind Engineering and Industrial Aerodynamics 99 (2011) 1011–1024.

[27] H. Kozmar, L. Procino, A. Borsani, G. Bartoli, Sheltering efficiency of wind barriers on bridges, Journal of Wind Engineering and Industrial Aerodynamics 107-108 (2012) 274–284.

[28] X.-Z. Li, M. Wang, J. Xiao, Q.-Y. Zou, D.-J. Liu, Experimental study on aerodynamic characteristics of high-speed train on a truss bridge: A moving model test, Journal of Wind Engineering and Industrial Aerodynamics 179 (2018) 26–38.

[29] M. Wang, X.-Z. Li, J. Xiao, Q.-Y. Zou, H.-Q. Sha, An experimental analysis of the aerodynamic characteristics of a high-speed train on a bridge under crosswinds, Journal of Wind Engineering and Industrial Aerodynamics 177 (2018) 92–100.

[30] H. Xiang, Y. Li, S. Chen, G. Houb, Wind loads of moving vehicle on bridge with solid wind barrier, Engineering Structures 156 (2018) 188–196.

[31] H. Xiang, Y. Li, S. Chen, C. Li, A wind tunnel test method on aerodynamic characteristics of moving vehicles under crosswinds, Journal of Wind Engineering and Industrial Aerodynamics 163 (2017) 15–23.

[32] M. Suzuki, K. Tanemoto, T. Maeda, Aerodynamic characteristics of train/vehicles under cross winds, Journal of Wind Engineering and Industrial Aerodynamics 91 (2003) 209–218.

[33] L. Zhu, L. Li, Y. Xu, Q. Zhu, Wind tunnel investigations of aerodynamic coefficients of road vehicles on bridge deck, Journal of Fluids and Structures 30 (2012) 35–50.

[34] F. Xue, Y. Han, Y. Zou, X. He, S. Chen, Effects of wind-barrier parameters on dynamic responses of wind-road vehicle–bridge system, Journal of Wind Engineering and Industrial Aerodynamics 206 (2020) 104367.

[35] J. Bettle, A. Holloway, J. Venart, A computational study of the aerodynamic forces acting on a tractor-trailer vehicle on a bridge in cross-wind, Journal of Wind Engineering and Industrial Aerodynamics 91 (2003) 573–592.

[36] A. Alonso-Estébanez, J. D. C. Díaz, F. Álvarez Rabanal, P. Pascual-Munoz, Numerical simulation of bus aerodynamics on several classes of bridge decks, Engineering Applications of Computational Fluid Mechanics 11 (1) (2017) 435–449.

[37] EN 1317-1: Terminology and general criteria for test methods (2010).

[38] OpenFOAM, User manual, version 10, https://openfoam.org (2022).

[39] B. Launder, D. Spalding, The numerical computation of turbulent flows, Computer Methods in Applied Mechanics and Engineering 3 (1974) 269–289.

[40] S. Patankar, D. Spalding, A calculation procedure for heat, mass and momentum transfer in three-dimensional parabolic flows, International Journal of Heat and Mass Transfer 15 (1972) 1787–1806.

[41] D. Sykes, A new wind tunnel for industrial aerodynamics, Journal of Wind Engineering and Industrial Aerodynamics 2 (1977) 65–78.

[42] EN 1991: Actions on structures - Part 1-4: General actions - Wind actions (2005).

[43] S. Charuvisit, K. Kimura, Y. Fujino, Experimental and semi-analytical studies on the aerodynamic forces acting on a vehicle passing through the wake of a bridge tower in cross wind, Journal of Wind Engineering and Industrial Aerodynamics 92 (2004) 749–780.

[44] M. Sterling, A. Quinn, D. Hargreaves, F. Cheli, E. Sabbioni, G. Tomasini, D. Delaunay, C. Baker, H. Morvan, A comparison of different methods to evaluate the wind induced forces on a high sided lorry, Journal of Wind Engineering and Industrial Aerodynamics 98 (2010) 10–20.

[45] M. Batista, M. Perkovic, A simple static analysis of moving road vehicle under cross wind, Journal of Wind Engineering and Industrial Aerodynamics 128 (2014) 105–113.

[46] F. Cheli, R. Corrado, E. Sabbioni, G. Tomasini, Wind tunnel tests on heavy road vehicles: Cross wind induced loads - part 1, Journal of Wind Engineering and Industrial Aerodynamics 99 (2011) 1000–1010.